

A Computational Framework for Modelling Biomechanical Tumour Dynamics and Tissue Interactions: A Proof-of-Concept in Pleural Mesothelioma

Sacha Gijsbers^{1,2}[0009-0007-8326-8123], Valeria Krzhizhanovskaya¹[0000-0002-8247-129X], Stefano Trebeschi^{2,3}[0000-0002-5714-289X], and Vivek M. Sheraton^{1*}[0000-0002-6577-6016]

¹ Computational Science Lab, Informatics Institute, University of Amsterdam, The Netherlands

² Department of Radiology, The Netherlands Cancer Institute – Antoni van Leeuwenhoek Hospital, Amsterdam, The Netherlands

³ GROW – Research Institute for Oncology & Reproduction, Maastricht University, Maastricht, the Netherlands

* Corresponding author: v.s.muniraj@uva.nl

Abstract. In Malignant Pleural Mesothelioma (MPM), solid stress and tissue deformation significantly impact tumour growth and invasion. This study presents a computational framework that integrates biomechanical tumour dynamics, tissue deformation, and force interactions within a realistic anatomical setting. Using the Finite Element Method, the framework is applied to a lung mesh reconstructed from CT scans, incorporating a synthetic mesothelioma tumour with defined material properties. Numerical results from the simulations closely match the analytical solution, with deviations within 5%, confirming the model’s reliability and accuracy. Simulations of point compression and surface expansion effectively capture the localised tumour deformation and lung volume changes, replicating expected breathing mechanics under different conditions. The findings emphasize the role of mechanical interactions in tumour progression, demonstrating how increased tissue stiffness affects deformation patterns and respiratory dynamics. This study establishes a foundation for integrating computational biomechanics with predictive tumour modelling, offering potential applications in personalised medicine for MPM.

Keywords: Finite Element Method · Tumor biomechanics · Malignant Pleural Mesothelioma · Tissue deformation

1 Introduction

Cancer is one of the leading global health challenges, with growing mortality rates. In 2020, approximately 10 million deaths, or roughly 16% deaths worldwide, were attributed to cancer [31]. Cancer growth displaces and disrupts the

normal functioning of healthy organs and tissues, contributing to organ failure and eventual death. One of the tumours that most exemplify this is Malignant Pleural Mesothelioma, also known as MPM. MPM is an aggressive lung cancer. MPM originates from the pleura, a thin membrane lining the lungs and thoracic cavity. It typically spreads in a crescent-shaped pattern, encasing the lung and exerting external pressure on both the lung and the mediastinum [16]. Overall, patient's survival after diagnosis is estimated to be between 4 to 12 months, with some multimodal therapies extending life expectancy to 5 years for 3% to 18% of patients [16]. Biomechanical modelling of tumour interactions with surrounding structures is essential but has often been overlooked, even in cases where its impact is evident, such as in malignant pleural mesothelioma. Therefore, it is critical to advance knowledge about the mechanisms involved in MPM tumour dynamics and the interplay with the surrounding environment in order to develop better treatment options and patient outcomes [23].

Multiple models have been developed to study tumour dynamics and treatment response. They can be divided into three types: discrete, continuum, and hybrid models. Discrete models focus on individual cells or groups of cells, used for cell signalling studies, while ignoring tissue mechanics [23]. Continuum models describe tumours as multi-phase systems using differential equations but lack single-cell resolution [12]. Lastly, the hybrid models combine both approaches, such as modelling cells individually while treating extracellular components as the continuum model [24]. While these models have advanced our understanding of tumour biology, they primarily focus on the microenvironment ignoring the macro-scale mechanical interactions between tumours and their surrounding tissues [26]. For example, tumours can deform adjacent organs or alter physiological functions (e.g., lung expansion during breathing), but this interaction is usually not modelled explicitly. Moreover, biomechanics plays a crucial role in tumour progression. In a realistic anatomical context, mechanical forces would stir the tumour into a growth path of least resistance [8], while causing tissue deformation, impairment of organ functioning and friction between the surrounding tissues [17]. This interplay of mechanical forces, alongside biochemical and biological factors, plays a crucial role in the onset, development, diagnosis, and treatment of cancer. Tumours, like other biological tissues, are subjected to various mechanical forces, which impact cellular function and behaviour [3]. These changes create a complex landscape where both cancer cells and surrounding tissues exhibit distinct physical abnormalities, directly impacting tumour behaviour and its response to treatments [17].

The transition from medical imaging to computational modelling follows a structured process of scanning, geometric reconstruction, and meshing. CT and MRI scans capture high-resolution tumour and lung structures, which are then processed for segmentation. Deep learning-based methods [30] have enhanced automation and accuracy in identifying anatomical features. Computational models automate meshing and predictive tasks, enhancing efficiency while preserving anatomical detail [32]. AI-driven models further support structural analy-

sis, patient-specific simulations, and treatment planning, advancing personalized medicine [5].

One significant biomechanical factor is solid stress, an influential component within the tumour environment that plays a crucial role in cancer initiation, aggressiveness, and metastasis. While other mechanical stresses, such as interstitial fluid pressure (IFP), exist within the tumour microenvironment, solid stress is particularly important as it directly influences tumour growth and interactions with surrounding tissues [22]. Moreover, stresses like IFP and others, including fluid-induced shear stress and hydrostatic pressure, can be directly modelled within the current framework by extending the governing equations to incorporate fluid-structure interactions and pressure-driven deformations. Given its pivotal role in tumour progression, incorporating solid stress into predictive models is essential for improving diagnostic and therapeutic strategies [11].

In this study, this gap will be addressed by developing a computational framework to model tumour dynamics and tissue interactions, with a specific focus on mesothelioma. To investigate the deformation behaviours of lung tissue and tumours, the framework will be benchmarked using simple geometries subjected to compressive and tensile forces, allowing for an initial assessment of mechanical properties. These tests will be compared against analytical solutions to evaluate model performance. Building on this foundation, the model is extended to a realistic anatomical structure: a lung mesh derived from CT scans, with a synthetic mesothelioma tumour modelled as a sheet surrounding the lung. Point compression will be applied to the tumour to simulate forces from surrounding structures, while surface expansion within the lung will mimic breathing mechanics. By testing various deformation scenarios and implementing different elasticity models, this study aims to explore how mechanical forces impact the structural integrity and functionality of these biological structures.

2 Methods

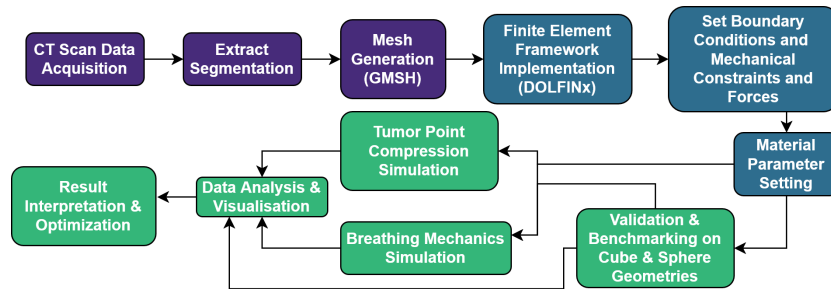


Fig. 1. Overview of the computational workflow for modelling tumour dynamics and tissue interactions. The process consists of data preprocessing, model implementation, simulations, and result analysis, with different colours indicating distinct stages.

Fig. 1 illustrates the key steps of the computational framework, from data acquisition and mesh generation to finite element simulations and result analysis, highlighting the integration of different modelling approaches for benchmarking, validation, and biological scenario testing.

2.1 Mathematical formulation of the elasticity model

In this section, we present the mathematical equations that form the basis of the computational framework, focusing on the elastic deformation of materials [6].

Linear elasticity PDE: using the Navier-Cauchy equations for small deformations can be written as:

$$-\nabla\sigma = f \quad \text{in } \Omega \quad (1a)$$

$$\sigma = \lambda \operatorname{tr}(\varepsilon)I + 2\mu\varepsilon \quad (1b)$$

$$\varepsilon = \frac{1}{2}(\nabla u + \nabla u^T) \quad (1c)$$

where σ is the stress tensor, f is the body force per unit volume, λ and μ are Lamé's elasticity parameters for the material in Ω , I is the identity tensor, tr is the trace operator on a tensor, ε is the symmetric strain tensor (symmetric gradient), and u is the displacement vector field. Above we have assumed isotropic elastic conditions [7, 21].

Variational formulation: consists of forming the inner product of the Eq.1. Which is gathered by deriving the weak form by integrating the linear elasticity equation against a test function and applying integration by parts [10]. This results in:

$$a = \int_{\Omega} \sigma(u) : \nabla v \, d\Omega \quad (2)$$

Analytical solution: used in the simulation is based on uniaxial stress-strain relations from Hooke's Law, resulting in the following reaction force:

$$F_{\text{analytical}} = S \cdot A = \frac{E \cdot \Delta h}{H} \cdot A \quad (3)$$

where $F_{\text{analytical}}$ is the analytically computed force, S is the applied stress, A is the cross-sectional area, E is Young's modulus representing the material's stiffness, Δh is the applied deformation or step size, and H is the initial height of the material. This assumes a simple linear relationship between stress and strain in a homogeneous material under uniform loading, which aligns with the small deformation assumption in the finite element implementation [9].

2.2 Simulation case studies

Three unique cases were analysed and simulated in the study. This section summarises the methods utilised for simulating and analysing these cases.

Cube Compression and Stretching: In this simulation, the deformation of a cube under compression and stretching was analysed for varying amounts of total deformation, compared to an analytical solution to serve as a benchmark of the simulation. The deformation was applied in three steps: 10%, 50%, and approximately 100% of the cube's total height. The total deformation was applied uniformly on the cube. An analytical solution based on uniaxial stress-strain relations from Hooke's Law was compared to the resulting deformation. The results were then displayed in a corresponding load-deflection curve was recorded for both the numerical and analytical solution. The numerical and analytical solutions will closely match if the maximum margin of error is below the 5% for numerical approximations [33]. The deformed shapes of the cubes for each deformation level were also visualised.

Tumour Point Compression: The goal of this simulation is to investigate how point compression affects the deformation behaviour of a tumour mesh, later to be used to simulate the tumour-environment interactions. The sphere geometry was compressed at the top, to show how point compression works on simple geometries. After which, a bundle of points were selected, at extreme ends of the tumour mesh, as selecting one point is too small to have a visible impact. The deformation was applied at two levels: 10% and 20% deformation of the total height of the tumour mesh. Point compression was applied at the top and side of the mesh with different total deformation constraints. And at two points of the mesh, to show how multiple point compression can be performed simultaneously.

Lung surface Extension: The third simulation involves modelling the stretching of surfaces on a cube to represent the surfaces that will also be selected in the lung mesh and the expected result of the expansion. In this simulation, 4 sides and the bottom of the cube and lung meshes are selected to be expanded. For the lung model, 20% of the lung width was selected for each side and bottom surfaces, with only a few of the highest points fixed to prevent displacement. Additionally, 30% of the lung width was selected for the side and bottom surfaces to observe the impact of surface selection on the deformation behaviour. The simulation was coupled with compression to model the breath cycle, and the corresponding changes in volume were plotted. To demonstrate the versatility of the model, the elasticity parameters were adjusted, and a non-linear, stiffer material model was introduced, in which E is scaled with strain. The more strain, the stiffer the model. This allowed for exploration of different material behaviours, showing how the simulation can be adapted for varying conditions. The volume rate of change during the breath cycle was also analysed.

2.3 Finite element simulation

The finite element method (FEM) is a numerical technique for solving partial differential equations (PDEs) over complex geometries by discretizing the domain into smaller elements. *FEniCSx* an open-source platform designed for FEM simulations due to its automatic differentiation is used in this study [1]. *DOLFINx*, the *C++/Python* interface and the back-end of *FEniCSx0.9*, were used for modelling. It provides the core functionality for mesh handling, function spaces, and solving PDEs [13, 14]. A third-order Lagrange finite element space was employed to achieve higher accuracy in the numerical simulations.

Simulation parameters and material properties: To perform the simulations, material properties for the tumour and lung tissues were selected based on reported values in the literature. These properties include the Young’s modulus (E) and Poisson’s ratio (ν), which were used to calculate the Lamé parameters (λ , μ) in equation 1b.

Table 1. Material properties used in the simulations, including Young’s modulus (E) and Poisson’s ratio (ν) for tumour and lung tissues. The table also specifies the simulation domain size, mesh resolution, and relevant references.

Tissue Type	E [Pa]	ν	Domain Size (mm)	Mesh Cells	References
Tumour	10^5	0.3	[161 × 161 × 273.52]	5, 922, 906	[17, 25, 20]
Lung	10^4	0.3	[147 × 147 × 267.89]	3, 032, 524	[25, 20]
Lung (Non-linear)	$10^4 - 10^8$	0.3	[147 × 147 × 267.89]	3, 032, 524	[25, 20]

The table summarises the material properties used in Eq.1, for the simulations, E and ν for tumour and lung tissues. For normal lung tissue, a constant E of 10 kPa was chosen [25]. For non-linear lung tissue, E is assumed to increase with stress, reflecting the strain-dependent stiffening typical of lung tissue, especially under larger deformations or pathological conditions. Tumour tissue is modelled with a higher E of 100 kPa, simulating the stiffness of fibrotic or advanced tumours [17]. A Poisson’s ratio of 0.3 was used for both tissues, reflecting their near-incompressibility [25, 20].

Mesh generation

Mesh definitions for unit cube and sphere: A structured unit cube mesh was generated using *DOLFINx*’s built-in meshing capabilities as a benchmark model. The domain, $[0, 1] \times [0, 1] \times [0, 1]$, was discretized into a hexahedral mesh, which consists of small cube-shaped elements. After which, the cube was uniformly divided into 12 elements along all axis, resulting in a total of 1,728 elements [14]. A sphere tetrahedral mesh was created using Gmsh, allowing for

finer meshing control compared to FEniCSx's native tools and a complex shape compared to the cube. The meshes were converted to XDMF format for use in FEniCSx simulations.

Tumour and lung mesh definitions: Open-source CT scan data was used from the Cancer Imaging Archive [2], with *TotalSegmentator* [28] employed to extract the right lung instead of the left, as seen in Fig. 2a. The right lung was chosen due to its larger volume and three-lobe structure, making it a better candidate for studying tumour interactions. The segmented lung was processed to

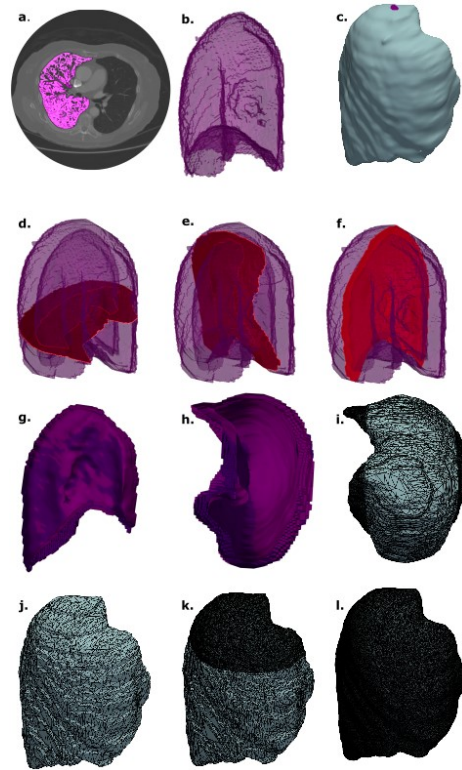


Fig. 2. (a) CT scan used to extract lung segmentation, with the right lung highlighted in magenta. (b) Tetrahedral mesh of the segmented right lung. (c) Synthetic tumour mesh, with the purple point indicating the top of the tumour used for compression simulations. (d)-(f) Cross-section images of the tumour, showing the empty space inside, representing the space occupied by the lung. (g)-(h) Cut surfaces of the tumour to visualise internal structures. (i) High-resolution sides of the tumour for surface expansion simulations. (j) Downsampled mesh with 5% of the original points for computational efficiency. (k) High-resolution region at the top of the tumour for point compression simulations. (l) Full-resolution tumour mesh.

ensure accurate voxel spacing for further mesh generation. The segmented lung data was converted into a tetrahedral mesh using *Gmsh*, see Fig. 2b. Surface extraction was performed using marching cubes, followed by mesh simplification and repair to ensure watertightness, meaning the mesh is completely enclosed without holes or gaps, making it suitable for simulations and further processing. The refined surface was then imported into *Gmsh*, where a surface loop and volume definition enabled high-quality mesh generation. Mesh parameters were adjusted to optimise curvature adaptation, and the final mesh was exported to *XDMF* format for use in *FEniCSx* simulations. A synthetic tumour was created encasing the segmented right lung based on the crescent-like mesothelioma growth patterns, see Fig. 2c. The tumour was generated using morphological dilation operations to simulate realistic spread, ensuring it remained confined to 2cm outside the lung, making it a significant sized tumour. See Fig. 2d-f for cross sections of the tumour and Fig. 2g & e, for the cut tumour, to see the inside structures. To optimise computational efficiency, the segmentation was down-sampled to 5% of the original number of points (see Fig. 2j for the downsampled mesh and Fig. 2l for high resolution mesh) while maintaining high resolution in regions where pressure would be applied. The same *Gmsh*-based meshing process was applied to the tumour segmentation to ensure consistency in the tetrahedral mesh. The final meshes maintained high-resolution regions where mechanical stress would be applied while optimising computational efficiency, see Fig. 2i & k.

3 Results

3.1 Benchmark simulation results on a unit cube

The results of the cube compression and extension simulations are shown in Fig. 3, where the deformation patterns and load-deflection curves are compared to the analytical solutions 3. Figures 3(a-c) illustrate the normalised displacement for three different compression levels: 10%, 50%, and 100% of the total height. Figures 3(g-i) show the deformation patterns for cube stretching at 10%, 50%, and 100% total extension. As expected, the deformation increases proportionally with the applied load. Figures 3(d-f & j-l) show the corresponding load-deflection curves, comparing the numerical (Eq.1) and analytical solutions (Eq. 3). Simulation results show a good agreement with the analytical solution, suggesting that the numerical method accurately captures the expected deformation behaviour. To quantify this, the maximum relative error between numerical linear elasticity solution and analytical solution of uniaxial stress-strain relations (from Hooke's Law) was calculated, revealing a consistent 4.68% error, well within the 5% requirement. All simulations exhibit the same error because the chosen linear elasticity model inherently scales proportionally with applied forces and deformations. The results demonstrate that the numerical model reliably predicts deformation under uniform loading and extension, ensuring sufficient mesh resolution and correctly applied boundary conditions, making it suitable for more complex simulations.

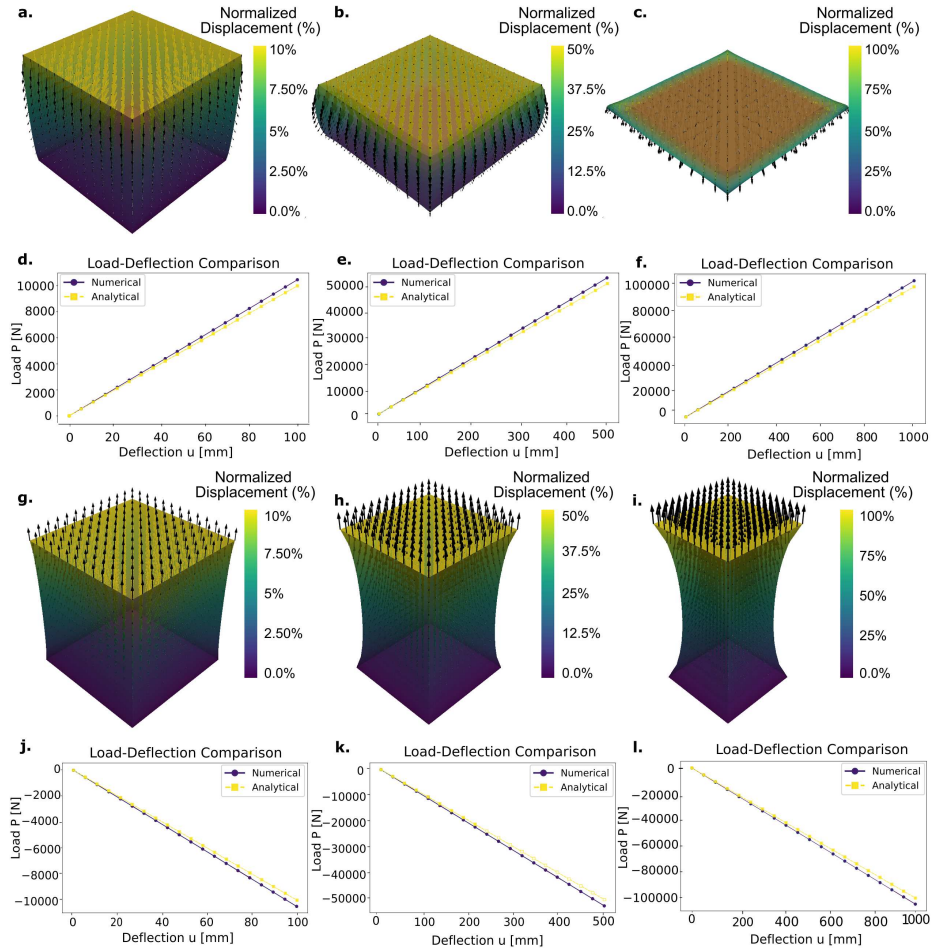


Fig. 3. (a-c) Normalised displacement for three different compression levels: 10%, 50%, and 100% of the total height. (g-i) Deformation patterns for cube stretching at 10%, 50%, and 100% total extension. The bottom of the cube remains fixed, and the displacement is visualised using a colour gradient, with higher displacement values at the top surface. Deformation increases proportionally with the applied load (d-f) and (j-l).

3.2 Tumour point compression simulation results

The point compression simulation was performed on a spherical geometry and a complex tumour mesh to analyse localised deformation. Applied forces and resulting displacements were recorded to assess the finite element model’s accuracy. In the spherical case, top compression caused a localised indentation with a maximum normalised displacement of 10%, showing smooth, symmetric deformation consistent with theory.

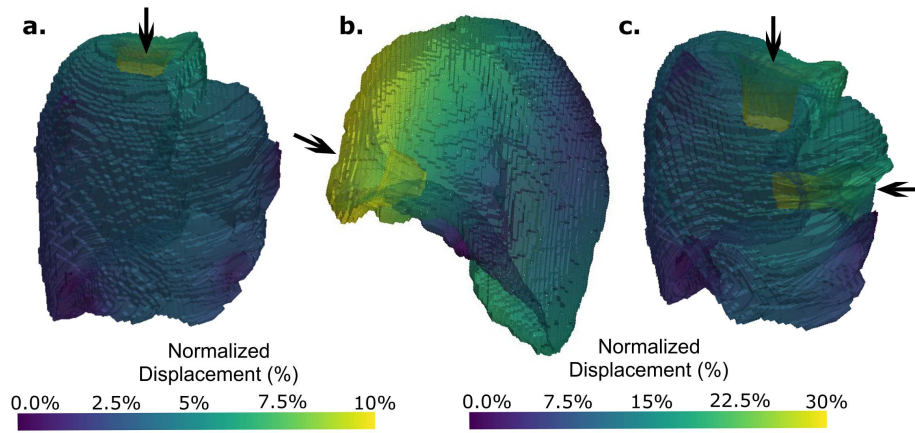


Fig. 4. (a) Tumour mesh under single-point compression at the top, producing a localised indentation with a maximum normalised displacement of 10% of the tumour’s total height. (b) Increased deformation magnitude and shifted compression location, showing asymmetric displacement distribution. (c) Multiple-point compression applied at the top and side of the tumour mesh, simulating complex loading conditions with maximum normalised displacement reaching 30%. The displacement is visualized using a colour gradient, where higher displacement values are represented in yellow and lower displacement values in purple.

The tumour mesh (Fig. 4b-d) was subjected to the single-point compression at the top, from one side and from 2 sides. The simulation tested different displacement magnitudes and locations. First, a small deformation (10% of the tumour’s total height) was applied (Fig. 4b), followed by an increase in deformation magnitude and a shift in the compression location to evaluate the response (Fig. 4c). The results confirmed that the implemented FEM correctly captured the expected indentation behaviour, with the displacement distribution smoothly radiating from the compression point. Fig. 4c shows the result of a single compression force at the side, testing the mesh’s response under asymmetric loading. This preliminary test ensured that the code correctly handled irregular geometries and non-uniform stress distributions before introducing more complex loading conditions. Once verified, multiple points were compressed simultaneously, as seen in Fig. 4d, to simulate realistic interactions in a biological environment. This is particularly relevant as surrounding structures in the body exert different forces at various locations on the tumour, forcing it to deform and adapt accordingly. Compression at the top and side of the mesh resulted in highly localised deformations, with maximum normalised displacement reaching 30% in the most compressed regions. Across all test cases, the numerical model accurately captured the expected deformation patterns, confirming its reliability for simulating soft tissue mechanics under localised compression.

3.3 Surface expansion simulation results

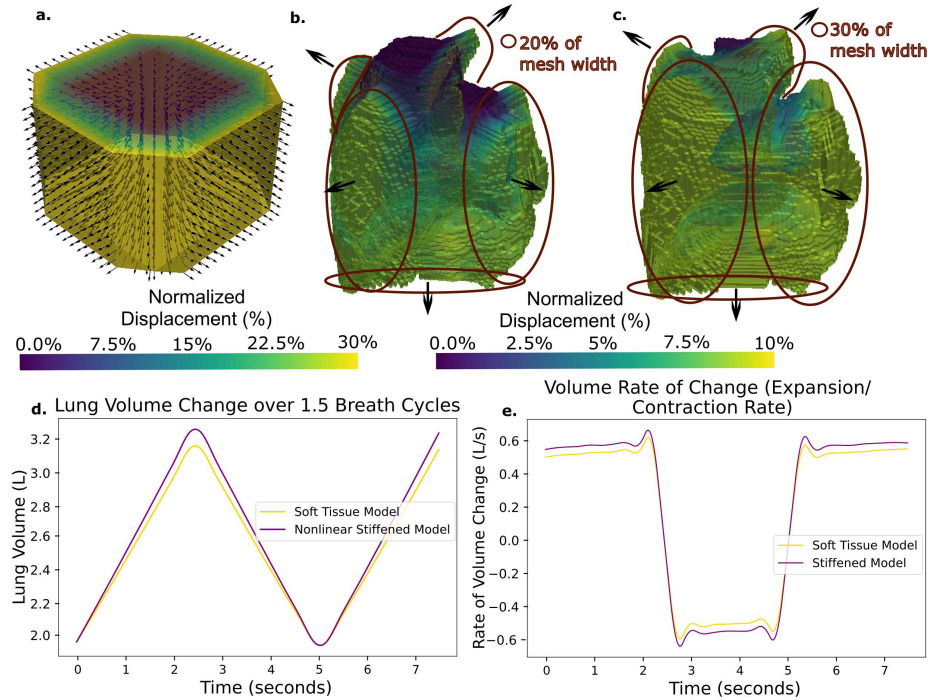


Fig. 5. (a) Expansion of selected surfaces in the lung mesh, illustrating the direction of expansion along four sides and the bottom surface, while the top surface remains fixed. (b, c) Applied expansion of 20% and 30% of the mesh surface width, respectively. The 20% expansion case shows localised deformation, whereas the 30% expansion leads to deformation across the entire lung. (d, e) Simulated lung volume and volume rate of change during breathing cycles.

The surface compression simulation simulated the expansion of surfaces in both the cube and lung models to analyse deformation behaviour under stretching forces. Figure 5a illustrates the expansion of selected surfaces in the lung mesh, showing the direction of expansion along four sides and the bottom surface, while the top surface remains fixed. The applied expansion was set to 20% and 30% of the mesh width, as shown in Fig. 5b & 5c, respectively. The 20% expansion case resulted in localised deformation, with some regions of the lung remaining nearly stationary. In contrast, the 30% expansion case produced deformation across the entire lung, suggesting a more realistic representation of breathing mechanics. Figures 5d & 5e show the corresponding lung volume and volume rate of change during simulated breathing cycles. The lung volume (Fig. 5d) follows a cyclic pattern with a sinusoidal-like curve, which is consistent with

the expansion and contraction dynamics expected in real pulmonary function. The volume rate of change (Fig. 5e) further confirms this behaviour, showing a smooth transition between phases of inhalation and exhalation. The stiffened model, see Fig. 5d & e, which incorporates a non-linear elasticity response, resulted in a more gradual expansion at higher deformations compared to the soft tissue model. The ability to simulate both linear and non-linear deformation allows for a detailed evaluation of how different material properties influence lung mechanics under expansion forces.

4 Discussion

The results highlight the effectiveness of point compression in simulating diverse pressure distributions on the tumour. This method provides a foundation for future simulations where mechanical forces can be scaled based on the densities and stiffness of surrounding tissues, allowing for a more realistic representation of tumour-environment interactions. Similarly, the lung volume change simulations followed expected physiological patterns, capturing key characteristics of normal respiration and forced respiration. The volume rate of change reflects the known asymmetric behaviour of inspiration and expiration due to airway resistance and lung tissue viscoelasticity, consistent with experimental findings [18]. The observed reduction in peak lung volume and slower rate of volume change in the stiffened lung model aligns with clinical studies on pulmonary fibrosis, where increased tissue stiffness leads to restricted expansion and airflow dynamics [25].

Lung tissue is inherently non-linear, and experimental studies have demonstrated that lung parenchyma does not behave as a simple linear elastic material. Instead, strain-dependent stiffening occurs due to collagen fibre engagement during deep inhalation [25]. The stiffened model in this study successfully captures this effect, improving its biomechanical accuracy. Additionally, the cyclic breathing pattern observed in the simulations suggests energy-efficient breathing dynamics, where tissue resistance at higher lung expansion mirrors real-life pulmonary mechanics [29]. The damping effects observed in the volume rate of change further support this accuracy, as lung tissue naturally absorbs mechanical energy to prevent damage under large deformations. This aligns with previous studies highlighting how lung mechanics involve both elasticity and resistance to rapid expansion/contraction [25].

Unlike existing continuum or hybrid models that rely on homogenized tissue properties or fixed boundary conditions [23], this model provides spatially resolved, patient-specific mechanical feedback from actual lung and tumour geometries. This enhances its ability to simulate local tissue deformation and mechanical impedance, critical for mesothelioma's heterogeneous, surface-bound growth patterns. Future versions should incorporate time-dependent tumour growth, driven by proliferative pressure, evolving stiffness, and mechanical feedback from the surrounding lung parenchyma, allowing for more dynamic, realistic growth. Integrating growth kinetics or coupling with cellular automata models could better simulate the spatial and temporal progression of mesothelioma. This would

not only help understand how increasing stiffness and tumour volume affect breathing mechanics but also identify the path of least growth resistance. By simulating tumour expansion, the model could pinpoint areas where the tumour is likely to grow with minimal resistance, aiding in treatment planning and surgical decision-making, including predicting tumour invasion and adaptation to mechanical changes.

A key application of this model lies in personalized medicine, where patient-specific tumour and lung geometries from medical imaging could be incorporated into individualized simulations [27]. Such models could improve predictions of tumour-tissue interactions, enabling more precise treatment strategies and surgical interventions tailored to a patient's unique biomechanical properties. Beyond oncology, the ability to simulate mechanical changes in diseased lungs has broader clinical implications. Conditions such as pulmonary fibrosis and chronic obstructive pulmonary disease (COPD) involve significant alterations in lung mechanics, which could be explored using similar modelling approaches. Understanding how stiffening or obstruction affects lung compliance may inform improved ventilation strategies in clinical settings [25, 4].

Expanding beyond biomechanics, integrating this model with biochemical processes such as nutrient transport, oxygen diffusion, and metabolic activity would provide a more comprehensive understanding of tumour-environment interactions [19]. Additionally, incorporating blood flow dynamics could enhance realism by accounting for vascular adaptations, such as tumour-induced angiogenesis or perfusion deficits in diseased lung tissue [15].

5 Conclusions

This study aimed to develop a computational framework based on linear elasticity to model tumour dynamics and tissue interactions, with a specific focus on mesothelioma. The approach was first validated using simple geometries, such as a cube and a sphere, subjected to compressive and tensile forces. By comparing the numerical results with analytical solutions, the model demonstrated strong accuracy, with numerical deviations staying within the expected 5% error margin. This validation confirms the reliability of the framework for further simulations involving more complex geometries and biological structures.

Beyond simple benchmarking tests, the model was extended to simulate tumour and lung interactions using point compression and surface expansion analyses. The point compression simulations on both spherical geometry and tumour mesh successfully captured localised deformation behaviour, confirming the model's ability to handle asymmetric and multi-point loading conditions. Additionally, the surface expansion simulations on the lung mesh demonstrated realistic breathing dynamics, with lung volume changes following expected cyclic patterns. The results indicate that the framework can effectively simulate soft tissue deformation and mechanical interactions, providing a strong foundation for modelling tumour progression and biomechanical responses.

While the current framework effectively captures fundamental tissue mechanics, it remains a simplistic model and requires further refinement to more accurately represent complex biological systems. More advanced testing, including the use of more difficult force equations beyond linear elasticity, is necessary for improving the model’s applicability to real-world scenarios. Future work will focus on incorporating additional mechanical properties, such as viscoelasticity and anisotropy, to better represent lung and tumour behaviour. The inclusion of patient-specific data from imaging techniques could further enhance the accuracy of simulations, making the model more relevant for MPM applications. This study sets a baseline from which these refinements can be made.

Acknowledgments. The authors acknowledge the National Cancer Institute and the Foundation for the National Institutes of Health, and their critical role in the creation of the free publicly available LIDC/IDRI Database used in this study. The authors would like to acknowledge the Research High Performance Computing (RHPC) facility of the Netherlands Cancer Institute (NKI).

References

1. Alnæs, M.S., Blechta, J., Hake, J. The FEniCS Project Version 1.5. *Archive of Numerical Software*, **3**. <https://doi.org/10.11588/ans.2015.100.20553> (2015)
2. Armato III, S.G., McLennan, G., Bidaut, L.: Data from lidc-idri (2015), <https://doi.org/10.7937/K9/TCIA.2015.LO9QL9SX>, the Cancer Imaging Archive
3. Bao, L., Kong, H., Ja, Y. The relationship between cancer and biomechanics. *Frontiers in Oncology*, **13**. <https://doi.org/10.3389/fonc.2023.1273154> (2023)
4. Bates, J.H., Irvin, C.G. Measuring lung function in mice: the phenotyping uncertainty principle. *Journal of applied physiology*, **94**(4), 1297–1306 (2003)
5. Bharati, S., Mondal, M., Podder, P. Deep learning for medical image registration: A comprehensive review. *arXiv preprint arXiv:2204.11341* (2022)
6. Bonet, J., Wood, R.D.: *Nonlinear continuum mechanics for finite element analysis*. Cambridge university press (1997)
7. Bower, A.F.: *Applied mechanics of solids*. CRC press (2009)
8. Esmaili, M., Stensjøen, A.L., Berntsen, E.M. The direction of tumour growth in glioblastoma patients. *Scientific reports*, **8**(1), 1199 (2018)
9. Huda, Z.: *Mechanical Behavior of Materials: Fundamentals, Analysis, and Calculations*. Springer Nature (2021)
10. Hughes, T.J.: *The finite element method: linear static and dynamic finite element analysis*. Courier Corporation (2003)
11. Islam, M.T., Righetti, R. A novel finite element model to assess the effect of solid stress inside tumors on elastographic normal strains and fluid pressure. *Journal of Engineering and Science in Medical Diagnostics and Therapy*, **2**(3), 031006 (2019)
12. Kaura, P., Mishra, T., Verma, N. Effects of combined chemotherapeutic drugs on the growth and survival of cancerous tumours—an in-silico study. *Journal of Computational Science*, **54**, 101421. <https://doi.org/https://doi.org/10.1016/j.jocs.2021.101421> (2021)
13. Logg, A., Wells, G.N. DOLFIN: Automated Finite Element Computing. *ACM Transactions on Mathematical Software*, **37**. <https://doi.org/10.1145/1731022.1731030> (2010)

14. Logg, A., Wells, G.N., Hake, J.: DOLFIN: a C++/Python Finite Element Library. In: Logg, A., Mardal, K.A., Wells, G.N. (eds.) *Automated Solution of Differential Equations by the Finite Element Method*, Lecture Notes in Computational Science and Engineering, vol. 84, chap. 10. Springer (2012)
15. McDougall, S.R., Anderson, A., Chaplain, M. Mathematical modelling of flow through vascular networks: implications for tumour-induced angiogenesis and chemotherapy strategies. *Bulletin of mathematical biology*, **64**(4), 673–702 (2002)
16. Napoli, F., Listì, A., Zambelli, V. Pathological characterization of tumor immune microenvironment (time) in malignant pleural mesothelioma. *Cancers*, **13**. <https://doi.org/10.3390/cancers13112564> (2021)
17. Nia, H., Munn, L., Jain, R. Physical traits of cancer. *Science*, **370**. <https://doi.org/10.1126/science.aaz0868> (2020)
18. Otis, A.B., McKerrow, C.B., Bartlett, R.A. Mechanical factors in distribution of pulmonary ventilation. *Journal of applied physiology*, **8**(4), 427–443 (1956)
19. Pries, A.R., Secomb, T.W.: Blood flow in microvascular networks. In: *Microcirculation*, pp. 3–36. Elsevier (2008)
20. Raveh Tilleman, T., Tilleman, M., Neumann, H. The elastic properties of cancerous skin: Poisson’s ratio and young’s modulus. *Optimization of Incisions in Cutaneous Surgery including Mohs’ Micrographic Surgery*, **105**(2) (2004)
21. Sadd, M.H.: *Elasticity: theory, applications, and numerics*. Academic Press (2009)
22. Sarntinoranont, M., Rooney, F., Ferrari, M. Interstitial stress and fluid pressure within a growing tumor. *Annals of biomedical engineering*, **31**, 327–335 (2003)
23. Sciumè, G., Gray, W., Ferrari, M. On computational modeling in tumor growth. *Archives of Computational Methods in Engineering*, **20**, 327–352 (2013)
24. Sheraton, M.V., Chiew, G.G.Y., Melnikov, V. Emergence of spatio-temporal variations in chemotherapeutic drug efficacy: in-vitro and in-silico 3d tumour spheroid studies. *BMC cancer*, **20**, 1–16 (2020)
25. Suki, B., Bates, J.H. Lung tissue mechanics as an emergent phenomenon. *Journal of applied physiology*, **110**(4), 1111–1118 (2011)
26. Sun, Y., Yao, J., Yang, L. Computational approach for deriving cancer progression roadmaps from static sample data. *Nucleic acids research*, **45**(9), e69–e69 (2017)
27. Viceconti, M., Henney, A., Morley-Fletcher, E. In silico clinical trials: how computer simulation will transform the biomedical industry. *International Journal of Clinical Trials*, **3**(2), 37–46 (2016)
28. Wasserthal, J., Breit, H.C., Meyer, M.T. Totalsegmentator: robust segmentation of 104 anatomic structures in ct images. *Radiology: Artificial Intelligence*, **5**(5), e230024 (2023)
29. Weibel, E.R., Hsia, C.C., Ochs, M. How much is there really? why stereology is essential in lung morphometry. *Journal of applied physiology*, **102**(1), 459–467 (2007)
30. Wilding, R., Sheraton, V.M., Soto, L. Deep learning applied to breast imaging classification and segmentation with human expert intervention. *Journal of Ultrasound*, pp. 1–8 (2022)
31. World Health Organization: Cancer (2020), <https://www.who.int/en/news-room/fact-sheets/detail/cancer>, accessed: 2025-02-22
32. Zhang, Z., Liu, Q., Wang, Y. Road extraction by deep residual u-net. *IEEE Geoscience and Remote Sensing Letters*, **15**(5), 749–753 (2018)
33. Zienkiewicz, O.C., Taylor, R.L.: *The Finite Element Method: Volume 1, The Basis*. Butterworth-Heinemann, 5th edn. (2000)